

Seismicity in the block mountains between Halle and Leipzig, Central Germany: centroid moment tensors, ground motion simulation, and felt intensities of two $M \approx 3$ earthquakes in 2015 and 2017

Torsten Dahm  · Sebastian Heimann ·
Sigward Funke · Siegfried Wendt · Ivo Rappsilber ·
Dino Bindi · Thomas Plenefisch · Fabrice Cotton

Received: 25 October 2017 / Accepted: 12 April 2018 / Published online: 16 May 2018
© Springer Science+Business Media B.V., part of Springer Nature 2018

Abstract On April 29, 2017 at 0:56 UTC (2:56 local time), an $M_W = 2.8$ earthquake struck the metropolitan area between Leipzig and Halle, Germany, near the small town of Markranstädt. The earthquake was felt within 50 km from the epicenter and reached a local intensity of $I_0 = IV$. Already in 2015 and only 15 km northwest of the epicenter, a $M_W = 3.2$ earthquake struck the area with a similar large felt radius and $I_0 =$

IV. More than 1.1 million people live in the region, and the unusual occurrence of the two earthquakes led to public attention, because the tectonic activity is unclear and induced earthquakes have occurred in neighboring regions. Historical earthquakes south of Leipzig had estimated magnitudes up to $M_W \approx 5$ and coincide with NW-SE striking crustal basement faults. We use different seismological methods to analyze the two recent earthquakes and discuss them in the context of the known tectonic structures and historical seismicity. Novel stochastic full waveform simulation and inversion approaches are adapted for the application to weak, local earthquakes, to analyze mechanisms and ground motions and their relation to observed intensities. We find NW-SE striking normal faulting mechanisms for both earthquakes and centroid depths of 26 and 29 km. The earthquakes are located where faults with large vertical offsets of several hundred meters and Hercynian strike have developed since the Mesozoic. We use a stochastic full waveform simulation to explain the local peak ground velocities and calibrate the method to simulate intensities. Since the area is densely populated and has sensitive infrastructure, we simulate scenarios assuming that a 12-km long fault segment between the two recent earthquakes is ruptured and study the impact of rupture parameters on ground motions and expected damage.

Electronic supplementary material The online version of this article (<https://doi.org/10.1007/s10950-018-9746-9>) contains supplementary material, which is available to authorized users.

T. Dahm (✉) · F. Cotton · S. Heimann · D. Bindi
GFZ German Research Centre for Geosciences,
Helmholtzstraße 7, 14467 Potsdam, Germany
e-mail: torsten.dahm@gfz-potsdam.de

T. Dahm · F. Cotton
Institute of Earth and Environmental Science,
University of Potsdam, Potsdam, Germany

S. Funke · S. Wendt
Institute for Geophysics and Geology, Leipzig University,
Leipzig, Germany

I. Rappsilber
Landesamt für Geologie und Bergwesen Sachsen-Anhalt,
Halle, Germany

T. Plenefisch
Federal Institute for Geosciences and Natural Resources,
Hannover, Germany

Keywords Deep crustal intraplate seismicity ·
Centroid moment tensor of $M \approx 3$ earthquakes ·
Observed and simulated ground motions

1 Introduction

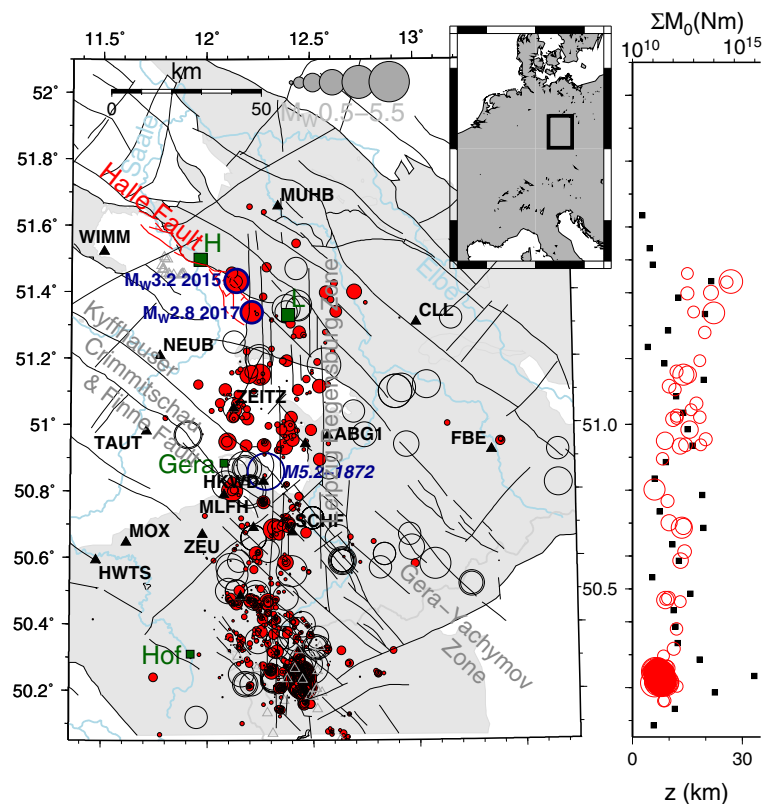
The seismicity in Central Germany occurs mostly in a N-S-oriented belt between 12° and $12^\circ 30'$ E longitude between the Vogtland/NW Bohemia region in the south and the cities Leipzig and Halle in the north (Fig. 1). The Vogtland/NW Bohemia region is characterized by earthquake swarms, occurring frequently (every 2–5 years since 1997) and in different spots (Korn et al. 2008; Fischer et al. 2014 see also right panel in Fig. 1). Maximum magnitudes of swarm earthquakes reached so far M 4.7 (21 Dec 1985, Table 3). More to the north, and close to the city of Gera, the largest historical earthquake of the last 700 years occurred on 6 March 1872, with maximum intensity of $I_0 = VII$ and estimated moment magnitude of $M_W = 5.2$ (see Table 3). This event, often called “Mitteldeutsches Beben,” was felt in Berlin (250 km), Breslau (350 km), Regensburg (240 km), Frankfurt (330 km), and Braunschweig (260 km) (von Seebach 1873).

The region north of Gera close to Leipzig and Halle was not affected by larger earthquakes ($I_0 > VI$) since

1553 (Torgau event). Reported events include three earthquakes close to Leipzig in 1905, 1914, and 1982 ($I_0 \approx IV - VI$) (Table 3 and Fig. 1). According to Leydecker (2011), there have been two earlier historical earthquakes in 827 and 1088 in northern Saxony with $I_0 = VIII/2$ (see also Grünthal et al. 1998; Grünthal and Wahlström 2012).

Instrumental seismic recordings in the region started in 1902 in Leipzig. Additional seismological observatories at station CLL (1935), MOX (1964) and BRG (1966), as well as installation of additional stations since 1985, improved monitoring capabilities gradually. In 1996 Seismologie-Verbund Mitteldeutschland, a collaboration between the geological surveys of Saxony, Thuringia, Saxony-Anhalt, and the Universities in Leipzig, Freiberg, Jena, and Dresden in cooperation with industry partners from mining (Wismut AG) and water supply (Landestalsperrenverwaltung Sachsen) established a modern and dense seismic monitoring network. In 2017, the joint network comprises more than 36 seismic stations including 20 permanent broad-band stations (some stations are covered by Fig. 1).

Fig. 1 Historical (open circles, $M_W > 3$) between 1326 and 2005, EMEC catalog from Grünthal and Wahlström (2012) and instrumental seismicity (2006–2017, $M_c < 1.5$, filled red circles) plotted with mapped tectonic faults (black lines) and distribution of uplifted basement blocks (gray-filled areas). Seismic stations are indicated by triangles (black-filled if broadband), and cities by green squares (L = Leipzig, H = Halle). The figure on the right side shows the moment release (black squares, 0.05° bins) between 2006 and 2017 and the depth of $M > 1.5$ earthquakes (open red circles) as a function of latitude



The magnitude of completeness of this modern network is $M_c = 0.5$. The instrumental seismicity since 2006 has epicenter location uncertainties of less than 2 km (68% probability) and confirms a diffuse pattern of seismicity in a N-S elongated zone between the city of Hof (Vogtland and NW-Bohemia region) and the cities of Halle and Leipzig. While the depth of earthquakes in the N-S elongated zone is systematically increasing towards north, the moment release shows maxima in Vogtland/NW-Bohemia, south of Gera and between Leipzig and Halle (Fig. 1).

The NS-oriented, diffuse zone of seismicity has been named the Leipzig-Regensburg Fault Zone (Kämpf and et al 1991; Bankwitz et al. 2003). However, the indications of NS-oriented basement faults are vague and have been only deduced from photo lineaments. The lineaments are not confirmed with modern satellite-based data in recent studies (Grünthal, pers. comm.). On the other hand, the study of gradients in geophysical potential field data (Becker et al. 1989) indicates that between Halle and Leipzig a bundle of shorter, N-S trending structures may exist, which have been interpreted close to Halle as possible faults.

The N-S zone of seismicity is crossed by NW-SE-oriented, major faults. The NW-SE orientation of basement faults is also evident from the trend of the boundaries of uplifted, tectonic blocks (Fig. 1). Some of these NW-SE-oriented faults were associated with larger historical earthquakes. Examples include the system of Kyffhäuser-Crimmitschau-Fault, the Finne-Fault and the Gera-Jachymov-Fault at the latitude of the city of Gera.

Sub-parallel faults at the latitude of Halle and Leipzig are for instance the well-known Halle fault system (Fig. 1 and Rappsilber 2006). It represents the boundary fault between the Halle-Wittenberg block in the north and the Merseburg block in the south. The Halle-Wittenberg block has been uplifted, so that the basement rocks are directly exposed or are covered by shallow Cenozoic sediments. Reflection seismic data indicate that the Halle-Wittenberg block was thrust on top of the Merseburg block, so that the structurally higher Merseburg block consisting of massive Mesozoic rocks is at a lower elevation. The measured vertical offset in the city of Halle is more than 1000 m. The Halle fault can be traced as a slightly curved feature in a SE direction towards the city of Leipzig, where the fault offset appears to diminish and the fault

develops several surface branches. Deep crustal seismic profiles have been measured 30 to 100 km west of Halle, e.g., the profiles ZENTROSEIS-THUBRA (Bormann and Bankwitz 1986) and DEKORP-BASIN 9601 (Krawczyk et al. 1999). However, the resolution and data density of these seismic lines does not allow for a clear conclusion in terms of dip and penetration depth of the Halle fault system. The large vertical offset indicates that the Halle and neighboring faults are major deep-reaching faults. So far, their potential to generate deep crustal earthquakes was unclear. As we discuss below, the location and source mechanisms of the 2015 and 2017 earthquakes can be related to the Halle and Leipzig system and indicate that the Mesozoic Halle faults may be re-activated between 20 and 30-km depth.

2 Earthquake source parameters

The mainshocks of the April 16, 2015 and April 29, 2017 earthquakes were recorded by local and regional seismic networks of Saxony (SX), Thuringia (TH) and the German regional seismic network (GR). For location, we use arrival times of P and S waves of 36 stations with distance of 140 km or less (Fig. 1). Stations at distances of more than 110 km recorded Pn phases as first arrivals and do not pose strong constraints on the event depth, but help to fill azimuthal gaps to better constrain the epicenter. For the 2017 earthquake, the largest azimuthal gap is 79°. The closest seismic stations are at about 26 km epicentral distance (Table 1). The arrival times are measured from unfiltered traces with sampling frequencies of 100 or 200 Hz. A local/regional velocity model is used for location (Table 4), which is based on the experience of the seismological surveys in Collm. For location, a Gauss gradient method is used: HYPOCENTER implemented in SEISAN (Ottemöller et al. 2016). Station corrections are not considered. The local magnitudes M_L of both events have been derived using the attenuation functions implemented in software packages SEISMIC HANDLER by the Federal Institute for Geosciences and Natural Resources (BGR) in Hannover (uses original tables by Richter 1958), and SEISAN (Ottemöller et al. 2016) by Leipzig University (Table 1 for details). The final locations from P- and S-wave arrival times and M_L values are given in Table 1.

Table 1 Hypocenter and centroid location of mainshocks and nearby seismicity

Event date and time (UTC)	Latitude (°N)	Longitude (°E)	Depth (km)	Magnitude (M_L for L, M_W for C)	r_{\min} (km)	
16-Apr-2015 06:38:09.3	51.434 ± 0.8 km	12.142 ± 1.1 km	26.8 ± 1.7	3.2 ± 0.4	36	L
	51.42 ± 1.1 km	12.13 ± 0.9 km	28.7 ± 1.6	3.20 ± 0.03		C
29-Apr-2017 00:56:23.7	51.340 ± 0.5 km	12.214 ± 0.9 km	22.3 ± 1.6	3.0 ± 0.2	26	L
	51.34 ± 2.2 km	12.21 ± 1.2 km	25.2 ± 1.9	2.80 ± 0.04		C
Nearby seismicity including aftershocks (location from Leipzig University)						
02-Nov-2011 01:19:23.2	51.380 ± 1.4 km	12.415 ± 1.7 km	11.1 ± 6.5	0.3 ± 0.3		L
14-Dec-2012 02:08:27.5	51.328 ± 1.2 km	12.335 ± 1.6 km	16.8 ± 4.2	0.3 ± 0.3	44	L
14-Dec-2012 02:31:53.6	51.338 ± 2.4 km	12.316 ± 3.7 km	16.1 ± 5.2	0.1 ± 0.3	45	L
16-Apr-2014 17:03:42.5	51.386 ± 0.9 km	12.270 ± 1.0 km	7 ± 2.3	1.0 ± 0.3	40	L
29-Jun-2014 00:12:01.1	51.403 ± 1.8 km	12.197 ± 3.3 km	19.9 ± 9	-0.1 ± 0.3	36	L
10-Feb-2015 01:46:45.0	51.475 ± 0.9 km	12.287 ± 1.0 km	16.2 ± 3.6	1.3 ± 0.2	21	L
16-Apr-2015 07:35:51.9	51.432 ± 0.8 km	12.141 ± 1.1 km	25.7 ± 2.0	1.7 ± 0.3	36	L
22-Aug-2015 19:28:55.0	51.334 ± 1.3 km	12.241 ± 1.4 km	15.0 ± 7.0	0.4 ± 0.3	32	L
09-Sep-2016 16:21:57.5	51.458 ± 0.8 km	12.120 ± 1.2 km	15.0 ± 4.1	1.6 ± 0.3	27	L
29-Apr-2017 23:37:07.4	51.342 ± 0.7 km	12.231 ± 1.5 km	19.1 ± 3.6	0.2 ± 0.3	36	L
20-Nov-2017 22:43:50.1	51.316 ± 0.5 km	12.311 ± 1.0 km	15.0 ± 4.6	0.6 ± 0.2	31	L

Uncertainties give 68% probability. L and C refer to solutions by Leipzig University and Centroid from moment tensor inversion, respectively. r_{\min} is the hypocenter distance to the closest station. M_L at Leipzig University is estimated by $M_L = 1.0 \cdot \lg(A) + 0.910 \cdot \lg(r) + 0.00087 \cdot r - 1.67$, where A is the peak-to-peak amplitude on horizontal components in nm, r the hypocentral distance and the logarithm is taken to the basis of 10

From 2006 to 2017, 11 additional earthquakes have been recorded in ± 15 km from both events (Fig. 2), with magnitudes ranging from $M_L = -0.1$ to 1.7 (Table 1). Thereof, one (2017) and two events (2015) can be interpreted as aftershocks. Waveforms of these aftershocks are similar to those of their mainshocks. The small number of aftershocks is not unusual for deep earthquakes ($z > 15$ km), as it is indicated in the area of the Northern Alpine Foreland and Lake Constance. However, the statistics there are still relatively poor and more data are needed for sound conclusions. The epicenters in Fig. 2 show a vague alignment with the trend of the NW-SE-oriented faults. Deepest events occur at the SW end along a profile perpendicular to the Halle fault (Fig. 2b).

2.1 First motion focal mechanism solutions

First motion polarities were measured at 14 (15) Pg and 21 (16) Pn phases for the 2015 (2017) events. These could be used to derive well-constrained first motion focal solutions, which for both events indicate normal faulting with a strike and dip of a common

nodal plane between 330° – 338° and 40° – 43° , respectively (Table 2, Fig. 3).

2.2 Moment tensor solutions

The moment tensor solutions are derived with a full waveform, probabilistic optimization method (referred to here as the BABO method, implemented as an open-source software in the seismic source optimization framework Grond, <http://gitext.gfz-potsdam.de/heimann/grond/>). It implements an efficient bootstrap-based method to retrieve solution sub-spaces, parameter trade-offs, and uncertainties in earthquake source parameter estimation problems. In our case, we considered restituted displacement waveforms of P and S phases filtered between 0.5 and 1.0 Hz for comparison with synthetic waveforms.

2.2.1 Forward modeling and objective function design

Synthetic waveforms are modeled based on pre-calculated Green's functions assuming the appropriate regional velocity profile from the CRUST 2.0

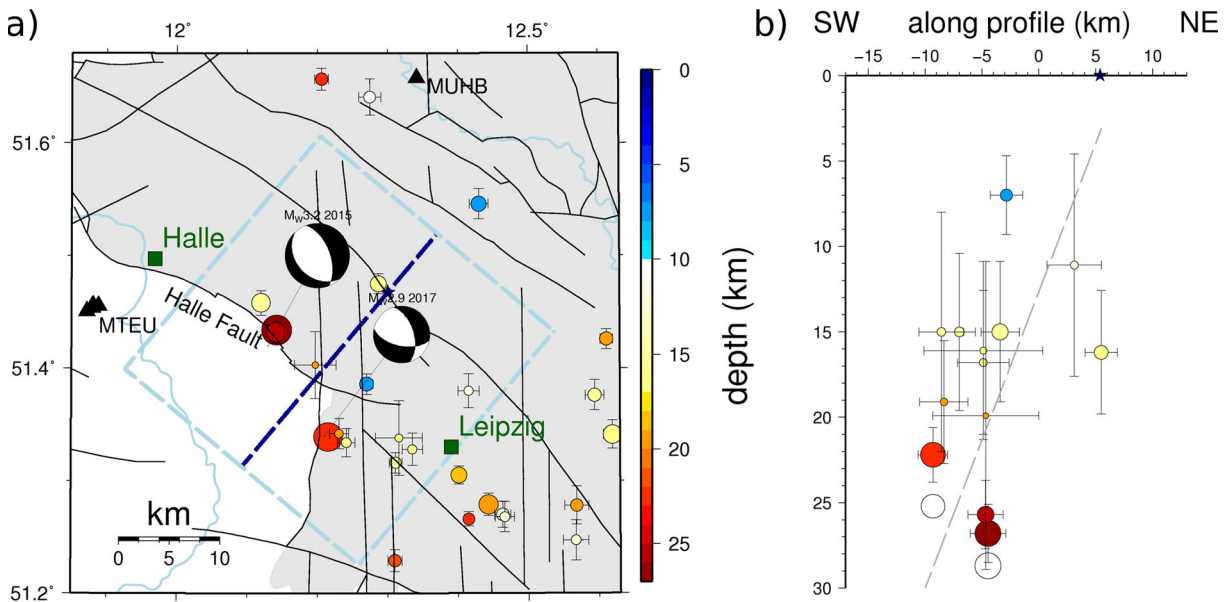


Fig. 2 **a** Zoomed epicenter map of the Leipzig–Halle region with the two best double couple solutions of the April 2015 and 2017 mainshocks. Filled circles show the location and depth of micro-earthquakes including aftershocks (see Table 1, catalog of Leipzig University at <http://uni-leipzig.de/collm/auswertung-temp.html>). Black triangles show nearest stations. **b** Cross section of hypocenters within the light-blue rectangle projected

onto the dark-blue line profile (blue star as reference point). The open circles indicate the projected centroid depth from the waveform inversion. The dashed line indicates a 60° dipping plane (note different scales for profile and depth), which would outcrop near the fault sub-parallel to the Halle fault near the reference point

Earth model database (see <http://igppweb.ucsd.edu/~gabi/crust2.html> and Bassin et al. (2000)). The Green’s functions (GF) were calculated with the orthonormal propagator method (using the program QSEIS, (Wang 1999), <https://github.com/pyrocko/fomosto-qseis/>), for a 1-km grid spacing from 1 to

140-km source-receiver distance and between 1- and 30-km source depth at 8-Hz sampling rate including near-field terms. Alternatively, the hybrid method by Wang et al. (2017) can be used to calculate GF. All GF’s are stored in a Pyrocko GF store (Pyrocko toolbox, Heimann et al. 2017) for efficient use during

Table 2 Source mechanisms

S_1°	D_1°	R_1°	S_2°	D_2°	R_2°	$(M_{nn}, M_{ee}, M_{dd}, M_{ne}, M_{nd}, M_{ed})/M_0$	M_0 in 10^{13}Nm	Method
26-Apr-2015 main shock								
330	40	-76	132	51	-101	$0.29 \pm 0.07, 0.58 \pm 0.11,$ $-0.87 \pm 0.09, 0.36 \pm 0.08,$ $0.025 \pm 0.15, 0.46 \pm 0.11$	7.0 ± 0.8	FM
339 ± 7	59 ± 4	-7 ± 10	135 ± 13	34 ± 5	-109 ± 14			MT
29-Apr-2017 main shock								
338	43	-42	101	63	-125	$0.38 \pm 0.16, 0.16 \pm 0.27,$ $-0.54 \pm 0.2, 0.62 \pm 0.09,$ $-0.31 \pm 0.18, 0.39 \pm 0.12$	1.7 ± 0.2	FM
340 ± 13	58 ± 8	-40 ± 23	101 ± 29	57 ± 11	-135 ± 21			MT

Orientation of best double couple (dc) with S = strike, D = dip, R = rake, M_{ij} = moment tensor components (normalized), M_0 = seismic moment in Nm. Method FM = first motion polarities, MT = full waveform moment tensor inversion of P- and S phases between 0.5 and 1 Hz

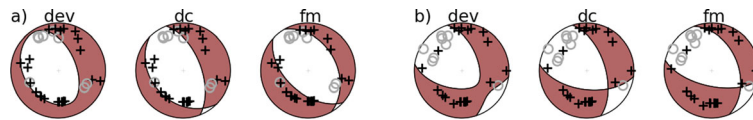


Fig. 3 Projection of the lower hemisphere of the P-wave radiation pattern of the deviatoric moment tensor (dev), best double couple (dc), and first motion polarities (fm). **a** Gives solutions for the 2015 and **b** for the 2017 main shock. The open circles and crosses represent downward and upward first motion polarities, respectively, projected on the lower hemisphere, where

take-off angles were calculated based on CRUST 2.0 model (Bassin et al. 2000). For the 2017 earthquake, a polarity of one station in ASSE was reversed. The locations of polarities in dev/dc and fm are slightly different because different depth and locations were considered for projection

the inversion. We use a nearest neighbor interpolation in between the grid points of the pre-computed GFs. Station amplification factors and transfer functions have been evaluated before the inversion using an empirical calibration method (Appendix B, Electronic Supplement). Data processing is applied to extract P- and S-phases at all stations. Restituted observed and synthetic ground displacement time series are filtered and windowed between $[-2 \text{ s}, +3 \text{ s}]$ from the expected phase arrival, given the tested candidate source model at each forward modeling step in the optimization. The L1 norm is used to measure the mismatch between observation and modeling. The optimal time shift for alignment between processed observed and synthetic waveforms are determined by grid search at each observation and tested source model. However, the maximal shift is constrained to $< 0.5 \text{ s}$ and a penalty misfit is added when shifting. Balancing weights are applied to the data to ensure an optimal weighting of different phases and distances (Heimann 2011). Weights are derived considering the average expected station/phase misfit value of random synthetics against observations set to zero. We empirically estimated them by forward modeling 1000 random source models prior to the optimization run. The weighted misfit contributions from all station and phase observations are combined into a global misfit value using the L1 norm and are normalized for convenience (see Heimann 2011, for details).

2.2.2 Optimization

Deviatoric moment tensors, centroid times and coordinates are estimated through an optimization algorithm. The source duration is not retrieved since we filter the observed and synthetic data below the corner frequency of the earthquake; thus, our source model

has nine degrees of freedom. We use 11 inversion parameters because we parameterize the moment tensor using its moment magnitude and six relative moment tensor entries and impose the deviatoric constraint during candidate source model generation.

The optimization algorithm is a Monte Carlo directed global search approach, with the non-standard ability to simultaneously and efficiently optimize an ensemble of perturbed objective functions. We use the Bayesian bootstrap method (Rubin 1981) to form the perturbations. Each perturbed variant of the objective function corresponds to a particular random choice of the set of bootstrap weights which are multiplied to the station and phase observation misfit contributions and are chosen so that they always sum up to one using the scheme of Rubin (1981). For comparison with standard single-objective function optimizations, we include the special case with equal bootstrap weights as one of the perturbed objective functions to simultaneously find a classical best fitting model.

Ideally, according to the Bayesian bootstrap method, the ensemble of solutions resulting from the perturbed optimizations should sample the posterior distribution of the source model parameters. In practice, mismodeling and violations of the independence of observational errors may introduce bias. Nevertheless, a great advantage of the bootstrap method over other approaches in error propagation is, that it implicitly accounts for modeling errors that affect every station/phase differently. Furthermore, it is conceptually simple and does not require any additional tuning parameters or statistical assumptions about the noise. It allows us to analyze the possible trade-offs, uncertainties, and ambiguities on the retrieved results.

In every step of the optimization, a new candidate source model is drawn from a dynamically updated

search space distribution and evaluated in every of the perturbed objective functions. In our case, only one forward modeling is required for every tested candidate model because the perturbed objective function values can be obtained by reweighting of intermediate values. The search space distribution starts as a uniform distribution in some user-defined source parameter bounds and is gradually narrowed down to the regions in model space yielding low values in any of the perturbed objective functions. The algorithm is capable of tracking multiple or irregularly shaped minima. The balance between explorativeness and convergence quickness can be tuned. All iteration steps and results are documented in a database. The result of the optimization is an ensemble of source models yielding low misfit values according to one or more of the perturbed objective functions. In a typical application, we select the N best from every of the M perturbation chains. In our case, $N = 10$ and $M = 100$ were chosen, yielding 1000 source models to draw statistics. A visual representation of the solution ensemble is shown as trade-off plots for our application in Figs. C.3–C.8 and C.9–C.14 in the Electronic Supplement.

The method has been successfully tested for synthetic case studies, earthquakes from mining and tectonic earthquakes in local and teleseismic distances (Cesca et al. 2017).

2.2.3 Application to the Leipzig earthquakes

For the analysis of the Leipzig earthquakes, we applied the BABO method as a mixed inversion of amplitude spectra together with time domain waveforms, with proper weighting, as well as a pure time domain waveform inversion. Both solutions are similar. Therefore, we discuss only the time domain solutions.

For the April 16, 2015 earthquake, we used P waves on vertical components (Z) at 15 broadband stations (BB, but SCHF with 5 s sensor) in distances between 34 and 94 km, and SH waves on the transversal components (T). For the April 29, 2017 earthquake, we could use 19 P and 18 S waves. The final solutions are given in Fig. 3 and Table 2. Figures 4 and 5 show examples of the waveform fit for the S and P waves for the $M_W = 3.2$ 2015 event. The signal to noise ratio (SNR) and the fits for the 2017 event are similar and presented in Appendix C in the Electronic

Supplement, together with plots to evaluate the trade-offs and uncertainties of individual parameters. Given the magnitudes of the studied events, the trade-offs between individual source parameters are small and parameters are well resolved. The solutions are stable. The moment magnitude of the 2015 and 2017 event are $M_W = 3.2 \pm 0.03$ and $M_W = 2.8 \pm 0.04$, respectively. Both centroid depths are with (28.7 ± 1.6) km for 2015 and (25.2 ± 1.9) km for 2017 slightly deeper than the first arrival hypocenters.

Such a systematic shift between first arrival and centroid location is quite common from our experience. Note that the waveform inversion has resolution power for the centroid location, because (i) time shifts are limited and penalty functions for shifts are applied, (ii) take-off angles and depth influence waveforms, and (iii) the hypocentral distances control absolute amplitudes. The double couple component is 66 and 91% for 2015 and 2017, respectively, and represented by a normal faulting mechanism with a strike of $(339 \pm 7)^\circ$ and $(340 \pm 13)^\circ$ and a dip of $(59 \pm 4)^\circ$ and $(58 \pm 8)^\circ$. Focal solutions based on first motion polarities are similar but show slightly smaller dip angles. Both have similar nodal planes, and the relative position of both events aligns with strike of the nodal plane. If we run the moment tensor inversion using the velocity model of Leipzig University (Table 4), the moment tensors change only little within the estimated uncertainties. The results indicate that both earthquakes, which occurred within about 15 km of each other, may have ruptured the same fault.

3 Macroseismic and instrumental ground motion data

The macroseismic intensities (Fig. 6) were derived from 107 and 177 felt reports for the April 16, 2015 $M_W = 3.2$ and the April 29, 2017 $M_W = 2.8$ earthquakes, respectively. The questionnaires were compiled by Seismologie-Verbund, applying the standard procedures for the collection of macroseismic data. Some questionnaires were obtained and shared by the BGR. The analysis is based on the European macroseismic intensity scale EMS-98 (Grünthal 1998), and the approach has been described for the 2015 event in Witthauer (2016). All intensity assignments were checked manually. Reports reflect noticeable shaking of many objects indoor, weak vibrations, and the

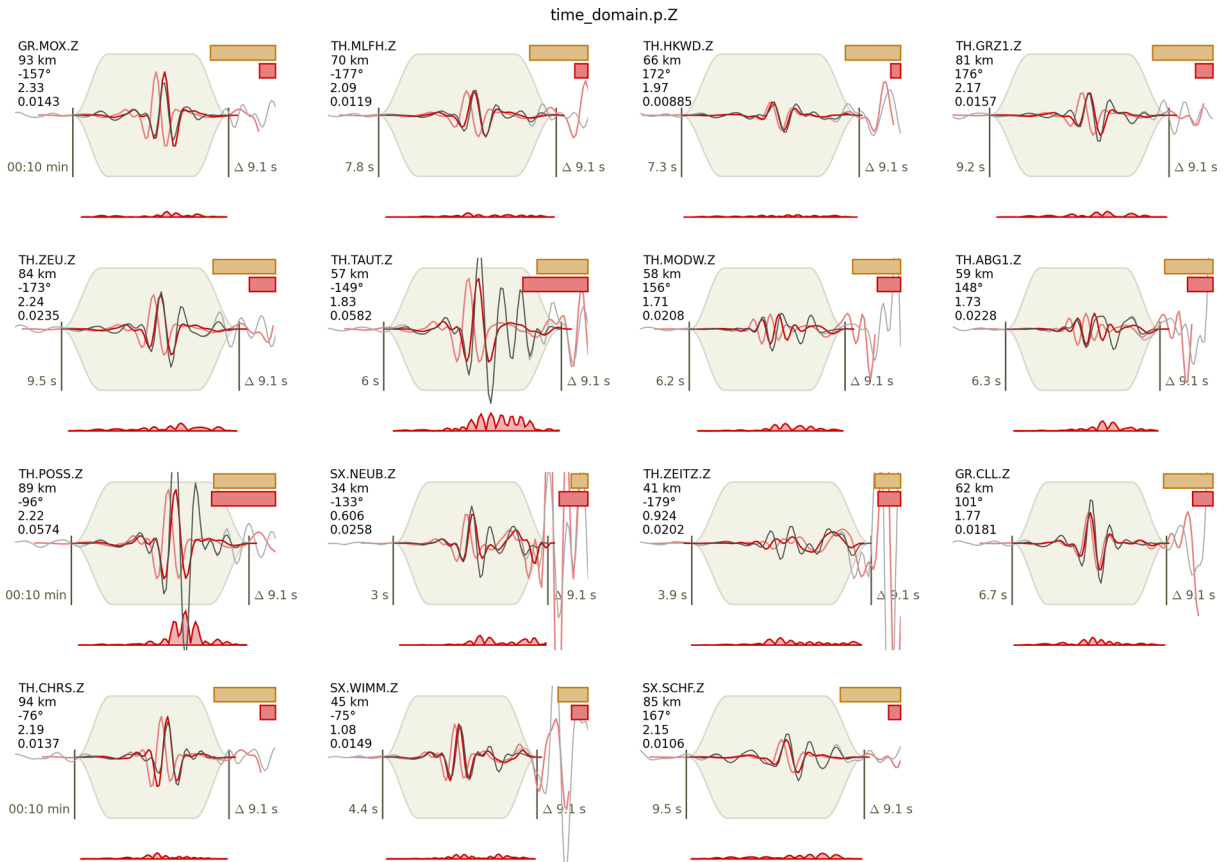


Fig. 4 Observed (black) and synthetic (red) waveforms of the P waves from the $M_W = 3.2$ 2015 earthquake. Light and strong colors indicate tapered and untapered data, respectively. Light red traces are unshifted, dark red are used final fits. Data are bandpass filtered to a frequency range between 0.5 and 1 Hz. Residuals are given by the red trace at the bottom of each graph. Relative weighting factors (balancing weights during inversion) and relative residuals are indicated by yellow and red bars,

respectively. The column of numbers give the station and channel name, distance r , azimuth, weighting factor, and relative residuals. The value printed on the left-hand side is the onset time with respect to event origin, the value printed on the right-hand side is the time interval between the two black marker lines. The flat part of the taper is 5 s. Traces are normalized after multiplication with their respective weighting factors

oscillation of hanging masses, etc. Structural damage was not reported, not even in the epicenter area. Interestingly, although both events were felt at distances more than 50 km, questionnaires indicate that inhabitants in some small districts close to the epicenters and with comparable site conditions and building structures have not felt the ground shaking. The quality of the assigned intensity IV is in general good. Intensities of III or II are difficult to detect, since the number of observations is often small leading to high uncertainties in the estimates. The area covered by intensity IV is 3370 and 2830 km² for the 2015 and 2017 earthquake, respectively. The similar size of the area measured for the 2017 earthquake, which was smaller

in magnitude, may be related to the smaller centroid depth of the 2017 earthquake.

We measured peak ground displacement (PGD), velocity (PGV), and acceleration (PGA) for the $M_W = 2.8$ April 2017 earthquake from all stations up to distances of 150 km. Peak measurements depend on the frequency range of the observed data. We picked PGV from low-pass filtered seismograms with different corner frequencies (f_c) and found that for the $M_W = 2.8$ April 2017 earthquake, PGV saturates for $f_c = 6$ Hz. This is in the range of the corner frequency of a $M_W = 3$ earthquake. In order to compare PGV to synthetic data, we finally applied a 1-stage band-pass filter between 0.5 and 6 Hz to both observed and

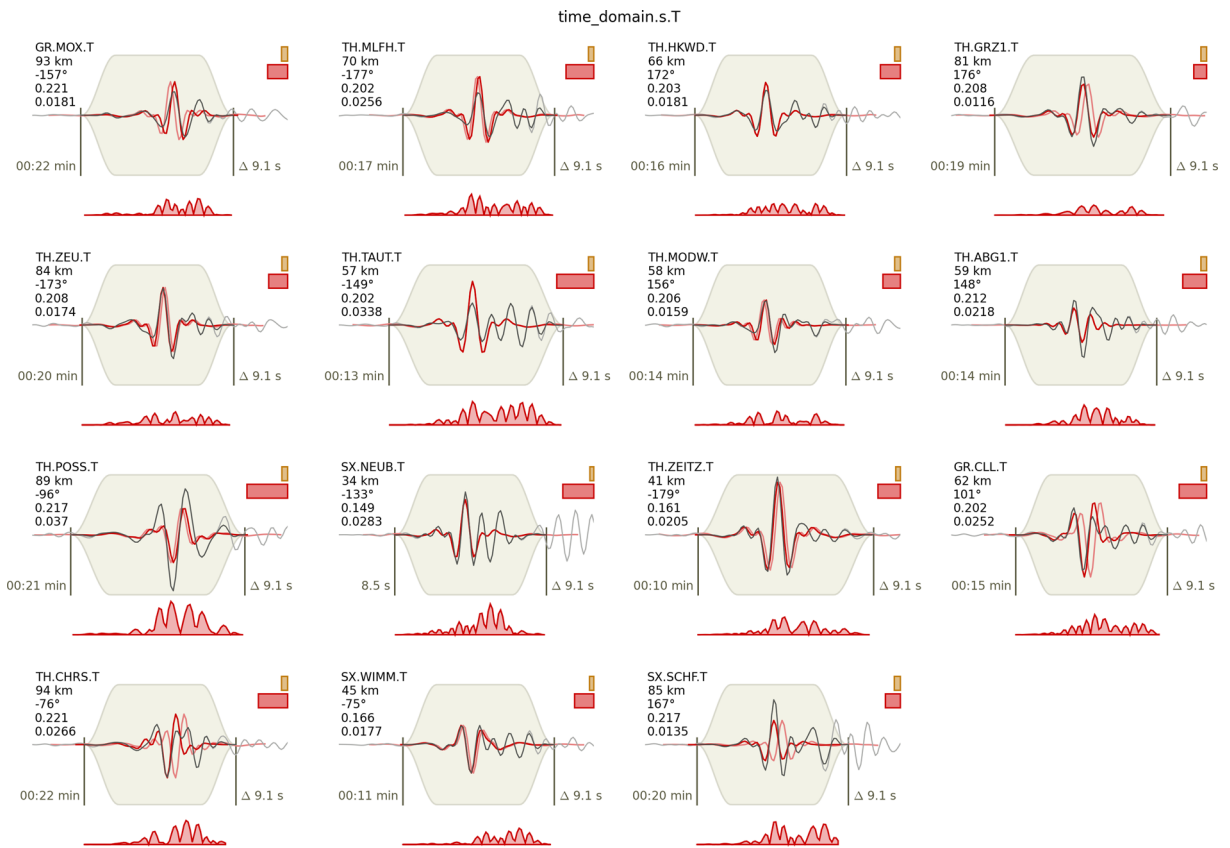


Fig. 5 Fit of the SH-waves from the $M_W = 3.2$ 2015 earthquake (see Fig. 4 for explanations)

synthetic velocity waveforms to automatically retrieve peak values, which we declare as PGV_{6Hz} . Note that for engineering problems, a frequency of 6 Hz is often too low. The largest PGV_{6Hz} at the closest stations in 30-km distance have values between 20 and 200 $\mu m/s$. The within-event scatter of measured PGV_{6Hz} is large (Fig. 7a) and is controlled by site, radiation pattern, attenuation, and wave type.

4 Ground motion modeling and scenario simulation

4.1 Ground motion

In order to simulate time histories, response spectra, and intensities for different earthquake scenarios, we need ground motion prediction (GMPE) and ground motion intensity conversion equations (GMICE). Average PGV distance curves are often simulated using regional stochastic models and GMPEs (Drouet

and Cotton 2015) and adding site and amplification factors for short-period and mid-period peak values (Wald et al. 2006). We use a different approach based on full synthetic waveforms. We simulate waveforms (Wang 1999) at distances between 0 and 200 km for a $M_W = 2.8$ and $M_W = 3.2$ earthquake in 20–30 km depth and with random radiation pattern. Sampling frequency was 16 Hz. We use the CRUST 2.0 model profile at the epicenter in two variants as end member models: (a) with a hard top layer of $v_p = 6.1$ km/s and $v_s = 3.5$ km/s, and (b) a soft top layer of 500-m thickness with $v_p = 2.5$ km/s and $v_s = 1.2$ km/s. Figure 7a compares the PGV_{6Hz} extracted from the ensemble of synthetic seismograms with the observed ones for the 2017 earthquake. Our simulations explain well the observed mean and scatter. Comparably good results are obtained for PGA_{6Hz} and PGD_{6Hz} and for the 2015 event. Introducing a soft layer of 500-m thickness beneath the stations (model b) leads to higher mean values of simulated PGV_{6Hz} (Fig. 7a, black dashed line), but does not change its scatter. We also plotted

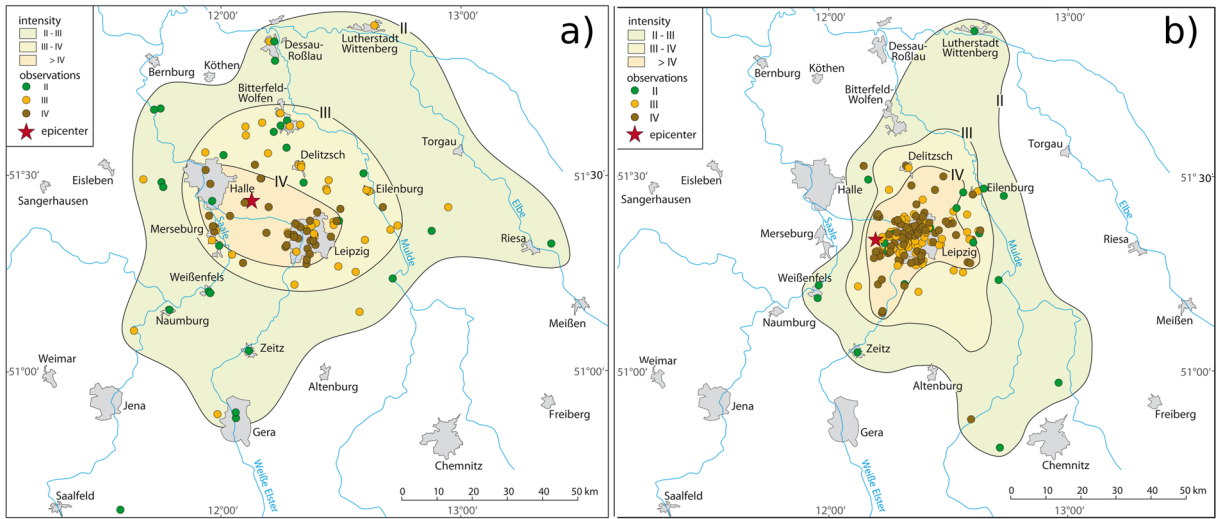


Fig. 6 Observed macroseismic intensities (Roman numerals) and felt zones for the April 16, 2015 $M_W = 3.2$ (a) and the April 29 2017 $M_W = 2.8$ (b) earthquakes. The colored circles

show average intensities in the local district derived from felt reports (see legend for scale). The colored polygons show the interpreted belts of intensity intervals

in Fig. 7a the ground motion prediction equations (GMPE) from two empirical models: (1) based on weak motions observed in the Lower Rhenish Shield, Germany, and the Netherlands (Hinzen 2005; Dost

et al. 2004), and (2) based on the Swiss Alpine model (Cauzzi et al. 2015). The two models either over- or underestimate the observed PGV_{6Hz} values for the Leipzig-Halle region (Fig. 7a, gray dashed lines).

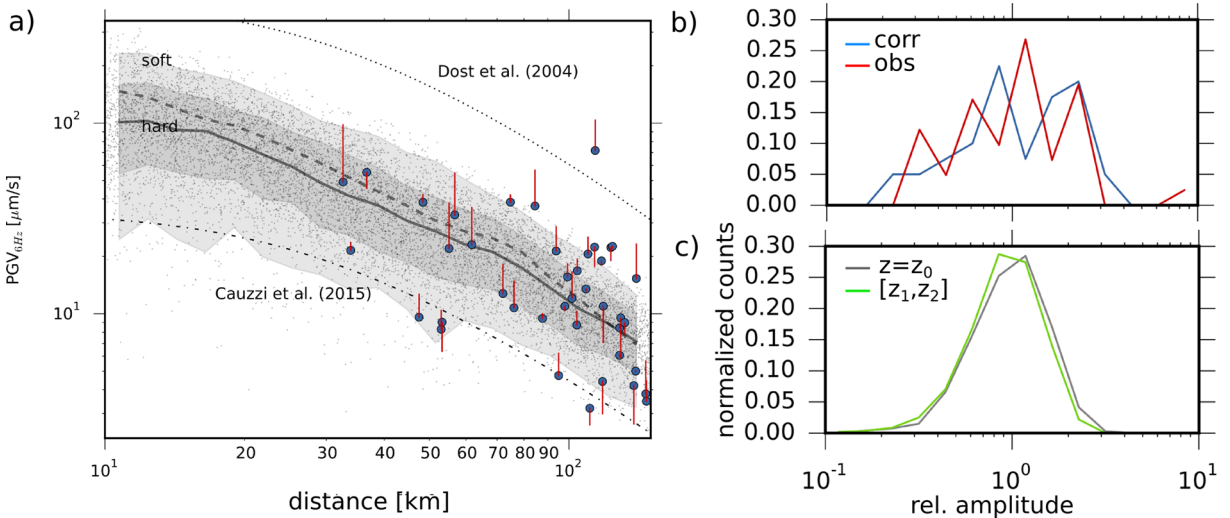


Fig. 7 a Observed (end of red lines opposite to blue circles) and radiation pattern corrected (blue circles) PGV_{6Hz} (0.5–6 Hz) are compared to PGV_{6Hz} extracted from full synthetic seismograms simulated for the $M_W = 2.8$ April 2017 earthquake. We simulated a random distribution of radiation patterns, source depth between 20 and 30 km, variable stress drop between 1 and 10 MPa and variable rupture velocity between 2250 and 3240 m/s (gray dots). Average (solid line) and 1σ and 2σ bands are indicated for a hard rock velocity model. The black dashed

line shows the average for the Earth model with a 500-m thick sediment layer on top. For comparison, the ground motion prediction equation from Cauzzi et al. (2015) (alpine structure) and from Dost et al. (2004) are plotted as dotted lines. b Scatter plot of the amplitude deviations from the average hard rock model, both for the raw (obs) and radiation pattern corrected data (corr). c Scatter of amplitudes for synthetic data for variable depth $[z_1, z_2]$ and fixed depth $z_0 = 25$ km, respectively

Figure 7b, c shows the scatter of the peak amplitudes relative to the average model, both for observed and synthetic waveforms, respectively. Normal distributions are indicated, with a \log_{10} standard deviation of 0.33 for observed PGV_{6Hz} and 0.29 for radiation pattern corrected PGV_{6Hz} data. The derived average model is similar to the median prediction of a GMPE and therefore the distribution of the residuals between the observed data and this average model can be compared GMPE within-event standard deviations. The obtained variability is similar to within-event standard deviations obtained recently in other regions (Drouet and Cotton 2015).

Different relationships between macroseismic intensities $I(x)$ (with $I_0 = I(x = 0)$) and PGA (Murphy and O’Brian 1977), PGV (Atkinson and Kaka 2006), spectral values (Ebel and Wald 2003) or Arias intensities are discussed in literature (Lesueur et al. 2013). Such a comparison assumes that the discrete distribution of observed intensities (given in Roman numbers) can be represented by a continuous function of equivalent intensities (given in arabic numbers). Lesueur et al. (2013) and others indicate that for weak ground motions the PGV is possibly a better proxy for intensity than PGA. We therefore only show results

for PGV. The comparison between equivalent I and PGV is not straight forward. Ground motion parameters are measured at specific sites. Macroseismic intensities represent effects averaged over a settled area.

The numbers of reports obtained for the $M \approx 3$ earthquakes at Leipzig and Halle are too small to average intensities in 10-km radii, as suggested by Lesueur et al. (2013). Additionally, the intensities are too small and outside the typical range where GMICEs have been calibrated. For instance, Fig. 8a shows GMICEs estimated in different regions using different interpolation models. For low PGV values, the predicted intensities are extremely heterogeneous and vary by 2 intensity units or more. Our observed intensities are larger than the intensities predicted by common GMICEs. In Fig. 8b, we plot the distance attenuation of intensities for the 2017 $M_W = 2.8$ earthquake in comparison to the predicted attenuation from our PGV_{6Hz} model, using the GMICE of Faenza and Michelini (2010). The attenuation with distance is well explained, even if the absolute values are too small. We assume that after calibration as in Fig. 8b the GMICE of Faenza and Michelini (2010) can be used in combination with our synthetic derived,

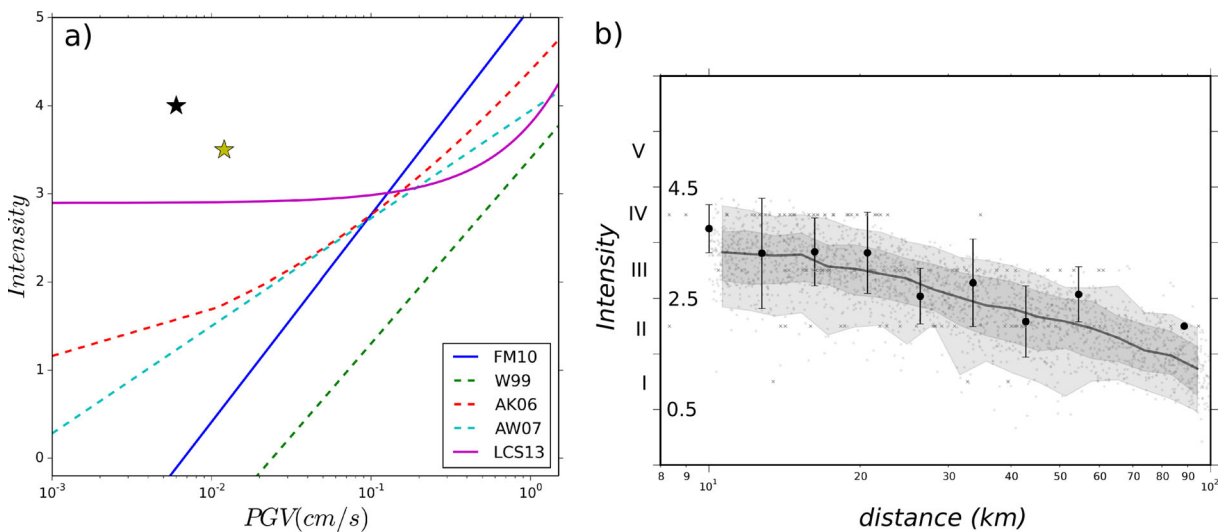


Fig. 8 a Comparison of different GMICEs in the range of weak PGV between 0.001 and 1 cm/s. The two stars indicate maximal PGV value (black) and the associated PGV value derived from our GMPE model (gray). Models in the legend refer to Faenza and Michelini (2010), (FM10), Wald et al. (1999), (W99), Atkinson and Kaka (2006), (AK06), Atkinson and Wald (2007), (AW07), and Lesueur et al. (2013), LCS13. **b**

Comparison of the attenuation of observed and simulated equivalent intensities (relative) using full waveforms (0.5–6 Hz) and the intensity—PGV relation (GMICE from Faenza and Michelini 2010). Note that we have corrected the equivalent intensities by a constant shift of 1.5 units down in order to compare them to the attenuation function

band-limited PGV_{6Hz} for simulating scenarios of weak earthquakes.

4.2 Rupture scenario simulation

We are interested in the scenario that the fault segment between the $M_W = 3.2$ 2015 and $M_W = 2.8$ 2017 earthquake would rupture in a single earthquake. The length of such a rupture would be about 12 km. We use the same depth and fault orientation as estimated for the April 2015 and 2017 earthquakes. If we assume a circular rupture with 6-km radius and a stress drop of 6 MPa the expected seismic moment is $\approx 2.9 \times 10^{18}$ Nm (Sato and Hirasawa 1973), associated with a moment magnitude of $M_W = 6.3$ and a corner frequency of 0.3 Hz (assumed rupture velocity 2.7 km/s). This is larger than the size of the 1578 and 1872 earthquakes close to Gera. We simulate a smaller rupture with radius of 2 km associated with a moment magnitude of $M_W = 5.3$ and a corner frequency of 0.9 Hz. Figures 9 and 10 show the simulated PGV_{6Hz} and intensity fields for the $M_W = 5.3$ simulation, both for hard rock and soft sediment top layer. Note that the processing is formally done up to 6 Hz, although the corner frequencies from the kinematic rupture model are smaller. The shake map simulations

using full waveforms contain a lot of details. Largest PGV_{6Hz} reach nearly 100 mm/s. The area affected by large PGVs is significantly increased if a soft sediment layer is modeled. Interesting is that the radiation pattern of S and surface waves resembles the patterns of high and low PGVs. For instance, the region close to the city of Bernburg is much less affected by high levels of ground shaking than Gera. If we assume a $M_W = 6.3$ instead of a $M_W = 5.3$ earthquake, the maximal PGVs exceed 230 mm/s. The intensities for the $M_W = 5.3$ lower crustal earthquakes were calculated from the GMICE of Faenza and Michellini (2010), both for a hard rock (Fig. 10a) and soft sediment upper layer (Fig. 10b). Ground motion is first felt by population at intensities of II, and no or only small damage is expected for intensities below V. Largest intensities are above VII, although the region affected is much larger for the soft layer simulation than for the hard rock scenario. Controlled by the radiation pattern, the city of Merseburg suffers from the largest intensities. An intensity of $I \approx 4$ is reached in some directions in more than 200 km from the epicenter. Overall, the population living in the $I \geq 4$ area exceeds 20 Mio inhabitants. The simulation indicates that about 1.6 Mio or 2.1 Mio people would be affected by equivalent intensities $I \geq 6$ if hard rock

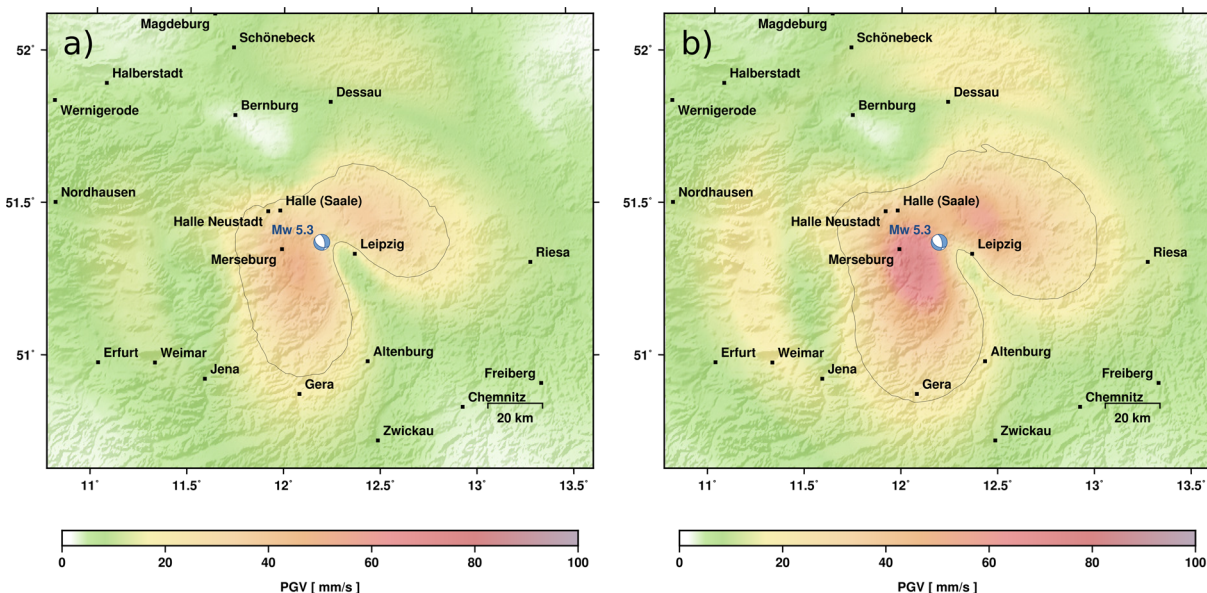


Fig. 9 Shake map scenario of a $M_W = 5.3$ characteristic lower crust earthquake in 25 km depth between Halle and Leipzig. **a** Predicted PGV_{6Hz} assuming hard rock upper layer

model. **b** Predicted PGV_{6Hz} assuming a 500-m thick soft layer beneath the surface with P and S velocities of 2.5 and 1.2 km/s, respectively. The contour line shows the 20 mm/s threshold

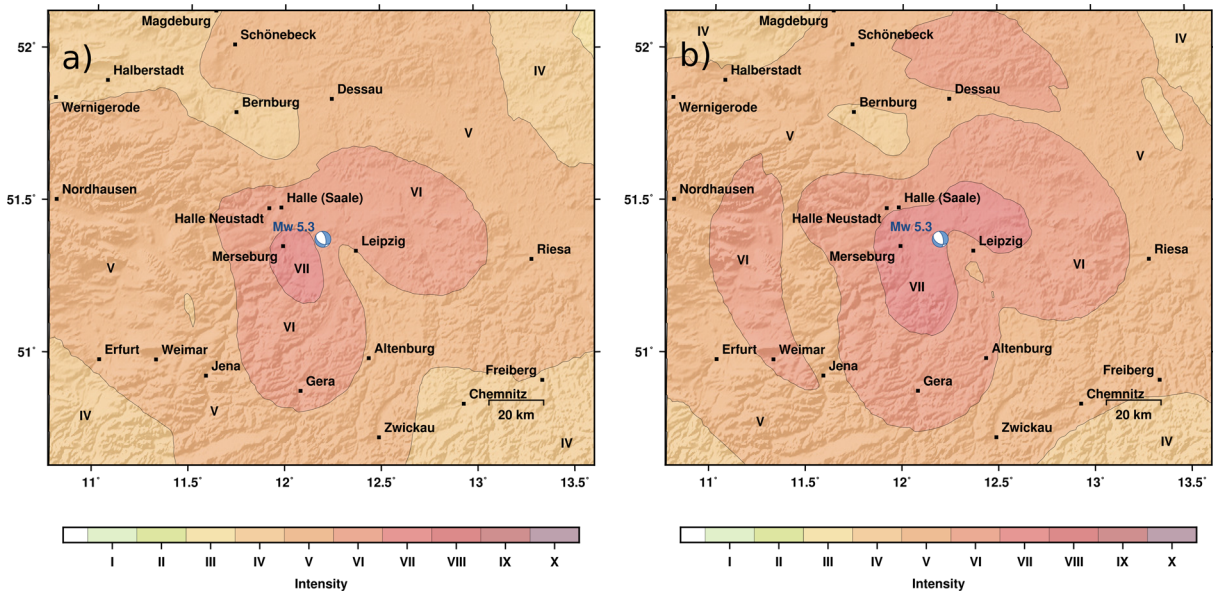


Fig. 10 Maps of predicted intensities for a $M_W = 5.3$ lower crust earthquake in 25-km depth, using the GMICE of Faenza and Michelini (2010) and assuming hard rock (a) and soft sediment (b) upper layers

or soft rock is assumed, respectively. If a $M_W = 6.3$ earthquake scenario is simulated, the largest expected equivalent intensities exceed 8.

5 Discussion

The $M_W = 3.2$ Gröbers 2015 and $M_W = 2.8$ Markranstädt 2017 earthquakes have unusual deep centroids at 29 and 26 km, indicating that they ruptured in the lower crust close to the Moho at a depth of about 31 km (Table 4). They both show normal faulting mechanisms with NW-SE striking nodal planes that have the same trend as major crustal faults, such as the Halle faults, between the cities of Leipzig and Halle. The relative positions of the epicenters align with the trend of the nodal planes and are 15 km apart. This indicates that both earthquakes may have ruptured the same fault in the lower crust. The distribution of nearby seismicity and aftershocks indicates that a SW dipping plane might have been reactivated. However, the number of detected aftershocks was small.

Leipzig was struck in the early instrumental time by a $M_W = 4.2$ ($I_0 = VI$, Table 3) earthquake on 27 June 1914. Since installation of modern monitoring stations in the 1980s, the region east of Leipzig experienced one earthquake with $M_W = 2.9$ on 20

February 1982 (Table 3). The historical record of felt earthquakes close to Leipzig goes back to about 800 Leydecker (2011), although the locations of Medieval events have to be taken with care. However, the historical record indicates that earthquakes with epicentral intensities of $I_0 = V$ and larger have occurred SE and close to Leipzig. The general trend of these historical earthquakes, as well as the micro-seismicity observed between Vogtland/NW Bohemia and Leipzig, is consistent with our hypothetical model that NW-SE striking fault systems are re-activated (Fig. 1). The system of the NW-SE trending faults (Hercynian orientation) in this part of Europe likely formed during and after the Variscan orogenesis, as a set of high angle normal faults crossing the major thrusts.

The present study is the first to derive moment tensor solutions for earthquakes close to Leipzig. The mechanisms clearly indicate that NW-SE trending faults have been activated. Known focal solutions of most of the earthquakes south of Leipzig and Halle indicate variations from normal faulting to strike slip faulting with nodal planes striking between N-S and NW-SE (Korn et al. 2008). The orientation of the nodal planes of the Gröbers 2015 and Markranstädt 2017 earthquakes is similar to the trend of the NW-SE Gera-Jachymov major fault. Summarizing the different information, we tend to postulate that the activation of NW-SE trending faults is typical for crustal

earthquakes in the region, and that earthquakes in the NS-oriented zone of enhanced seismic activity are not associated with major NS-oriented faults.

For instance, the belt of micro-earthquakes has a lateral extend of more than 150 km in NS direction, but no clear surface expressions of a NS-oriented fault over such a length. The earthquakes are relatively deep reaching the crust mantle boundary, indicating that stress is building up in the lower crust. For instance, lateral variability and transitions in the lithospheric thickness and strength can explain variations in the strain rate in the lower crust. Zones of increased strain and stress rates will depend on the shape and orientation of the sub-crustal heterogeneities. Both, the Bohemian Massive and the Franconian Line are lithosphere-scale units and boundaries with a potential influence on inner plate strain rates. High-resolution upper mantle tomography studies would be needed to prove such a model for the Halle Leipzig area

The earthquakes in 2015 and 2017 generated weak ground motions. Macroseismic intensities reached IV. As expected for the given magnitudes of $M \approx 3$ and the large depth of the hypocenters, no structural damage was reported. Maximal PGV and PGA measured in distances of ≈ 30 km reached 0.1 mm/s and 10 mm/s² at 6 Hz, respectively. We simulated PGV and PGA using a synthetic waveform stochastic approach. Our simulation explain the average values, the scatter, and the distance attenuation of observed PGV_{6Hz} (Fig. 7). The advantages of the waveform simulation approach are manifold. First, source parameters can be varied including the seismic moment, the stress drop, the orientation of faults and thus the radiation pattern, the rupture velocity (corner frequency), slip and directivity. Figure 7 gives an example of reduced residuals considering radiation pattern. However, as shown by previous studies, the conversion between SH and SV waves at scatter points leads to a smearing out of the radiation pattern in peak ground values at high frequencies (Takenaka et al. 2003; Castro et al. 2006). It is also interesting that for the synthetic waveforms the source depth has a much smaller effect on the scatter of the PGV_{6Hz} than the radiation pattern itself (Fig. 7b, c). Second, local velocity models can be considered in simulations and the approach can be transferred to regions in different settings. In our case, the CRUST 2.0 model has been used with a hard- and soft-top upper layer. And third, because of the efficient implementation based on

pre-calculated Green's functions, the stochastic simulation approach can be used to study scenarios in near real time.

Our simulations explain the scenario of a $M_W = 5.3$ earthquake rupturing the segment in between the 2015 and 2017 earthquakes. The estimated PGV's and intensities depend not only on magnitude but also on other source parameters. For instance, a shallower centroid depth increased the intensities in the epicentral regions. The variation of the stress drop has a large influence on the expected ground motions (Cotton et al. 2013) and thus on intensities and their variations. Our simulations show a large effect of the radiation pattern in combination with centroid depth, leading for instance to different distributions of the lobes and local spots of the expected high damage. However, absolute values of intensities depend on the GMICE. Mak et al. (2015) tried to validate intensity prediction equations for Italy by comparing eight regional models and a global GMICE model to five sets of Italian macroseismic intensity equations. As a surprise, the global model (Allen et al. 2012) performed equally well or better than all regional models showing the potential weaknesses of empirical models calibrated on limited datasets. This pointed to an important shortcoming of many GMPE and GMICE models in estimating realistic uncertainties. Our numerical Bayesian bootstrapping, full waveform approach considers uncertainties in PGV. The uncertainties from the stochastic variation the source parameter as centroid depth, radiation pattern, rupture velocity and stress drop are larger than the variations obtained from individual GMICE models. Therefore, a sophisticated regression analysis of GM parameter to derive slightly different GMPE and GMICE models is not further tried for the region of Leipzig and Halle. Instead, a better knowledge of velocity models, intrinsic attenuation at high frequencies, and characteristic rupture scenarios would help to reduce uncertainties of our shake map scenarios.

The assumed scenario of an $M_W = 5.3$ lower crustal earthquake and its implications can be compared with a "real" event of almost the same strength in Central Europe, namely the Roermond earthquake of 13. April 1992 in the Lower Rhine Embayment. The Roermond earthquake had a moment magnitude of $M_W = 5.3$ (Braunmiller et al. 1994). Its focal depth is between 15 and 21 km (depending on the locations of different agencies and authors) and is therefore likely already in the lower crust. The focal mechanism

is pure normal faulting striking in a NW-SE direction (Braunmiller et al. 1994; Oncescu et al. 1994). Thereby, all the source parameters (magnitude, focal depth, source mechanism) are similar to the chosen $M_W = 5.3$ scenario for the Leipzig/Halle area and implications of both, synthetic and real event, should be comparable. The calculated maximum intensity for the Roermond earthquake on the basis of the macroseismic observations was VII and the event was felt inside a radius around the epicentre of about 450 km. PGV measured at stations in BUG in 99 km and TNS in 209 km distance were 9.1 and 3.1 mm/s, respectively (Berger 1994). The estimated largest intensities for the $M_W = 5.3$ Leipzig/Halle scenario for hard and soft rock are slightly above VII (Fig. 10a, b) and thereby comparable to the maximum intensity VII of the Roermond earthquake. The extend of intensity IV in the scenario is partly more than 200 km from the epicentre, which is on same order as the Roermond earthquake for which the isoline of intensity IV is around 250 km from the epicentre (Camelbeeck and Eck 1994). Macroseismic and instrumental observations for the Roermond earthquake are comparable to the equivalent parameters in the synthetic estimations of an assumed $M_W = 5.3$ event in the Leipzig/Halle area indicating a reasonable choice of parameters in the synthetics. Since the 1992 Roermond earthquake caused substantial damage to houses in the boarder triangle of the Netherlands, Germany, and Belgium, it has to be expected that the occurrence of a comparable earthquake close to Leipzig/Halle would also lead to significant shaking and damage.

6 Summary

A novel, Bayesian-like full waveform inversion method was applied to retrieve source mechanism of two $M_W \approx 3$ earthquakes in the metropolitan region between Halle and Leipzig, Central Germany. The two events were the first natural earthquakes of this magnitude that occurred at the northern tip of a NS trending belt of increased seismicity between the Czech border and Leipzig since the 1905 and 1914 events. The earthquakes were also unusual because of their large depth indicating rupture in the lower crust close to the Moho. Our study obtained the first moment

tensor solutions in the region between Halle and Leipzig. They show for both earthquakes dominant double couple normal faulting mechanisms on faults striking NW-SE. From their relative position and locations and the distribution of nearby seismicity, we conclude that both events re-activated a SW dipping fault. SW dipping structures are known from geological mapping of larger Variscan fault systems in Central Germany. From comparison of the studied to historical and instrumental earthquakes in the NS-trending belt of enhanced seismicity, we postulate that the re-activation of NW-SE striking normal faults is a typical source mechanism. The reason of the enhanced earthquake productivity in a N-S trending belt and the increasing focal depth from S to N is, however, still enigmatic. We suggest that crustal and upper mantle heterogeneity may lead to a NS-oriented lobe of increased strain and stress rates

We devised a full synthetic waveform stochastic approach to simulate ground motion parameters. The comparison of synthetic and observed peak ground velocity shows that average and variability of peak values is well explained even using simple-layered Earth models. Based on the calibration dataset from the two $M \approx 3$ earthquakes, we simulate time dependent ground motions for a hypothetical, larger earthquake that would rupture the fault segment in the lower crust between the hypocenters of the two recent earthquakes. Our simulations indicate that such a rupture scenario would lead to strong peak ground velocities, and most probably to severe damage in the metropolitan areas of Leipzig and Halle. We suggest that more monitoring and research is performed to improve the preparedness and to mitigate the possible consequence of such an earthquake scenario.

Acknowledgements We thank the Grube Teutschenthal Sicherheits GmbH & Co. KG (GTS), Lausitzer und Mitteldeutsche Bergbau-Verwaltungsgesellschaft mbH (LMBV) and K-UTEC Salt Technologies AG for providing waveform data from Teutschenthal and Nachterstedt areas. Jens Skapinski shared felt reports collected on “Juskis Erdbebennews” with us, and Diethelm Kaiser from BGR provided some additional questionnaires. Nima Nooshiri is thanked for helping with Fig. 7a. We especially thank all helpers and staff running the excellent network of the Seismologie-Verbund in Central Germany. We are grateful to two anonymous reviewers who provided detailed and constructive reviews.

Appendix A: Historical earthquakes in the region and tables of used velocity models

Table 3 Historical earthquakes (1300–2000) with $I_0 > V$ (or $M_W > 4$) in the region between Halle-Leipzig and Vogtland/NW-Bohemia (LE=Leydecker (2011); GR=Grünthal and Wahlström (2012); S=Schwarz et al. (2010)). I_0 is the epicentral intensity, M_W is the transformed moment magnitude after S

Date	I_0	M_W	Lon E°	Lat N°	Location	LE	GR	S
1326	VI ^{1/2}	4.6	12.20	50.80	Gera	x	x	x
1332, 12 Feb	V ^{1/2}	4.0	12.20	50.80	Gera		x	x
1540, 26 Jun	VI ^{1/2}	4.6	12.90	51.10	N.Sachsen		x	x
1552, 6 Mar	VI	4.3	13.08	50.58	Annaberg-Buchholz		x	x
1552, 20 Apr	V ^{1/2}	4.0	12.66	50.57	Schneeberg		x	x
1553, 17 Aug	VI ^{1/2}	4.6	12.90	51.10	Torgau		x	x
1568, 26 Jul	V ^{1/2}	4.0	13.05	51.12	N-Sachsen			x
1578, 27 Apr	VI ^{1/2}	4.6	12.23	50.88	Gera		x	x
1598, 16 Dec	VI ^{1/2}	4.6	12.18	50.87	Gera		x	x
1616, 18 Dec	V ^{1/2}	4.0	12.25	51.20	Leipzig		x	x
1695, 18 Apr	V+	3.8	11.91	50.97	Eisenberg		x	x
1701, 27 Mar	V ^{1/2}	4.0	12.64	50.59	Schneeberg		x	x
1701, 8 Apr	V ^{1/2}	4.0	12.64	50.59	Schneeberg		x	x
1711, 25 Oct	VI	3.8	12.33	51.33	Leipzig			x
1720, 1 Jul	VI	4.3	12.40	50.56	Weissenfels	x	x	x
1770, 4 Nov	V ^{1/2}	4.0	12.43	50.25	Kraslice (CZ)		x	x
1771, 6 Jan	VI	4.3	12.43	50.25	Kraslice (CZ)		x	x
1789, 26 Aug	V ^{1/2}	3.7	12.12	50.55	Plauen		x	x
1811, 12 Dec	V ^{1/2}	3.9	12.97	50.63	Annaberg-Buchholz			x
1824, 13 Jan	V ^{1/2}	4.0	12.51	50.33	Kraslice (CZ)		x	x
1824, 19 Jan	VI ^{1/2}	3.8	12.40	50.20	Vogtland		x	x
1850, 15 Jul	V ^{1/2}	4.0	12.76	50.18	Sokolov (CZ)		x	x
1857, 7 Jun	V+	3.9	12.09	50.82	S of Gera		x	x
1872, 6 Mar 15:55	VII	5.2	12.28	50.86	Posterstein/Gera	x	x	x
1877, 5 Oct	V ^{1/2}	3.8	13.66	50.80	Erzgebirge			x
1896, 16 Mai	VI	4.3	12.30	50.50	Vogtland			x
1896, 3 Nov	V ^{1/2}	4.1	13.50	50.59	Erzgebirge			x
1897, 25 Oct 21:00	VI-	3.8	12.40	50.35	Zwota		x	x
1897, 29 Oct 19:45	VI+	4.2	12.48	50.35	Klingenthal		x	x
1897, 7 Nov 04:45	VI	4.3	12.50	50.30	Kraslice (CZ)		x	x
1897, 7 Nov 04:58	VI ^{1/2}	4.2	12.48	50.35	Klingenthal		x	x
1897, 17 Nov 06:30	VI	4.2	12.40	50.20	Vogtland		x	x
1897, 17 Nov 07:43	V ^{1/2}	4.0	12.32	50.22	Kraslice (CZ)			x
1900, 25 Jul 18:40	V ^{1/2}	3.8	12.45	50.35	Klingenthal		x	x
1903, 21 Feb 21:09	VI	4.1	12.47	50.34	S of Klingenthal		x	x
1903, 23 Feb 05:31	V ^{1/2}	3.7	12.42	50.30	SW of Klingenthal		x	x
1903, 25 Feb 23:11	VI	4.1	12.33	50.27	N of Bad Brambach		x	x
1903, 5 Mar 20:37	VI ^{1/2}	4.5	12.42	50.37	N of Zwota		x	x
1903, 5 Mar 20:55	VI ^{1/2}	4.6	12.42	50.37	N of Zwota		x	x
1903, 6 Mar 04:57	VI	4.2	12.47	50.34	S of Klingenthal		x	x

Table 3 (continued)

Date	I_0	M_w	Lon E°	Lat N°	Location	LE	GR	S
1903, 6 Mar 12:59	$V^{1/2}$	4.0	12.33	50.27	Landwüst		x	x
1903, 6 Mar 19:11	$V^{1/2}$	4.2	12.28	50.26	SE of Bad Elster		x	x
1903, 7 Mar 05:00	$V^{1/2}$	4.0	12.48	50.37	Klingenthal		x	x
1903, 7 Mar 05:01	VI	4.2	12.60	50.30	Vogtland			x
1903, 8 Mar 06:22	$V^{1/2}$	3.8	12.50	50.35	E of Klingenthal		x	x
1903, 27 Apr	VI	4.1	12.29	50.27	E of Bad Elster		x	
1905, 17 Aug	$V^{1/2}$	4.0	12.38	51.35	Leipzig	x	x	x
1908, 21 Oct 14:04	$V^{1/2}$	3.9	12.32	50.27	Landwüst		x	
1908, 21 Oct 20:39	VI	4.2	12.29	50.28	E of Bad Elster		x	
1908, 22 Oct 21:42	$V^{1/2}$	3.8	12.49	50.35	Klingenthal		x	
1908, 03 Nov 12:01	$V^{1/2}$	3.8	12.27	50.23	NW of Bad Brambach		x	
1908, 03 Nov 13:24	VI	4.2	12.31	50.23	N of Bad Brambach		x	
1908, 03 Nov 17:21	$VI^{1/2}$	4.5	12.47	50.34	S of Klingenthal		x	x
1908, 04 Nov 03:32	VI	4.1	12.49	50.36	Bad Klingenthal		x	x
1908, 04 Nov 10:55	$VI^{1/2}$	4.6	12.47	50.34	S of Klingenthal		x	x
1908, 04 Nov 13:10	$VI^{1/2}$	4.6	12.47	50.34	S of Klingenthal		x	x
1908, 04 Nov 20:41	VI	4.3	12.37	50.28	Wernitzgrün		x	x
1908, 06 Nov 04:35	$VI^{1/2}$	4.7	12.47	50.34	S of Klingenthal		x	x
1908, 12 Nov 11:31	$V^{1/2}$	4.1	12.40	50.40	Vogtland			x
1908, 19 Dec 05:03	$V^{1/2}$	3.2	12.39	51.11	Geringswalde			x
1911, 02 Apr 03:10	$V^{1/2}$	3.7	12.50	50.30	Vogtland			x
1911, 04 Apr 00:30	$V^{1/2}$	3.4	12.40	50.30	Vogtland			x
1914, 22 Apr 19:10	$V^{1/2}$	4.0	12.20	50.20	Vogtland			x
1914, 27 Jun	VI	4.2	12.43	51.36	Leipzig	x	x	x
1926, 28 Jan	VI	4.2	11.76	50.88	Gera		x	x
1929, 15 May 08:45	$V^{1/2}$	3.8	12.40	50.40	Vogtland			x
1982, 20 Feb 04:34	$\approx V$	2.9	12.44	51.32	Leipzig	x		x
1985, 14 Dec 05:38	$VI^{1/2}$	4.0	12.39	50.15	Novy Kostel (CZ)			x
1985, 21 Dec	VII	4.7	12.50	50.20	Novy Kostel (CZ)		x	x
1985, 24 Dec	$V^{1/2}$	4.0	12.45	50.24	Novy Kostel (CZ)		x	x
1986, 20 Jan	$VI^{1/2}$	4.4	12.45	50.24	Novy Kostel (CZ)		x	x

Table 4 Local (average, Leipzig University and Collm observatory) and crust 2.0 model used for centroid moment tensor inversion. We replace the first 0.5 km of the hard rock by the soft layer only for the soft rock test

Average model			CRUST 2.0 model with soft top layer		
Depth (km)	v_p (km/s)	v_s (km/s)	Depth (km)	v_p (km/s)	v_s (km/s)
0 – 12	5.8	3.35	(0 – 0.5	2.5	1.2)
12 – 23	6.7	3.87	0 – 10.5	6.1	3.5
23 – 31	6.9	3.98	10.5 – 20.5	6.3	3.6
31 – 50	7.7	4.45	20.5 – 31	6.6	3.6
50 – 80	7.9	4.56	31 – 80	8.04	4.48
80	8.3	4.79	80	8.05	4.49

References

- Allen TI, Wald D, Warden CB (2012) Intensity attenuation for active seismic regions. *J Seismol*. <https://doi.org/10.1007/s10950-012-9278-7>
- Atkinson GM, Kaka SI (2006) Relationships between felt intensity and instrumental ground motion for New Madrid ShakeMaps, Technical report. Department of Sciences, Carleton University, Ottawa
- Atkinson GM, Wald DJ (2007) "Did you feel it?" intensity data: a surprisingly good measure of earthquake ground motion. *Seismol Res Lett*. <https://doi.org/10.1785/gssrl.78.3.362>
- Bankwitz P, Schneider G, Kämpf H, Bankwitz E (2003) Structural characteristics of epicentral areas in Central Europe: study case Cheb Basin (Czech Republic). *J Geodyn* 35:5–32. [https://doi.org/10.1016/S0264-3707\(02\)00051-0](https://doi.org/10.1016/S0264-3707(02)00051-0)
- Bassin C, Laske G, Masters G (2000) The current limits of resolution for surface wave tomography in North America. *EOS Trans AGU* 81:F897
- Becker H, Lindner H, Schenke G, Schied G (1989) Mitteldeutsche schwelle/zentralteil - komplexbericht. VEB Geophysik, Leipzig (unpublished)
- Berger N (1994) Attenuation of seismic ground motion due to the 1992 Roermond earthquake, the Netherlands (extended abstract). *Geol Mijnb* 73:309–313
- Bormann P, Bankwitz P (eds) (1986) Komplexinterpretation des profilnetzes ZENTROSEIS abschlussbericht der SAD tiefenerkundung. Zentralinstitut für Physik der Erde, Potsdam (unpublished)
- Braunmiller J, Dahm T, Bonjer KP (1994) Source mechanism of the 1992 Roermond earthquake from surface-wave inversion of regional data. *Geophys J Int* 116:663–672. <https://doi.org/10.1111/j.1365-246X.1994.tb03288.x>
- Camelbeek T, Eck T (1994) The Roer Valley Graben earthquake of 13 April 1992 and its seismotectonic setting. *Terra Nova* 6:291–300. <https://doi.org/10.1111/j.1365-3121.1994.tb00499.x>
- Castro RR, Franceschina G, Pacor F, Bindi D, Luzi L (2006) Analysis of the frequency dependence of the S-wave radiation pattern from local earthquakes in Central Italy. *Bull Seismol Soc Am* 96:415–426. <https://doi.org/10.1785/0120050066>
- Cauzzi C, Edwards B, Fäh D, Clinton J, Wiemer S, Kästli P, Cua G, Giardini D (2015) New predictive equations and site amplification estimates for the next generation Swiss ShakeMaps. *Geophys J Int* 200:421–438. <https://doi.org/10.1093/gji/ggu404>
- Cesca S, Heimann S, Kriegerowski M, Saul J, Dahm T (2017) Moment tensor inversion for nuclear explosions: what can we learn from the 6 January and 9 September 2016 nuclear tests, North Korea? *Seismol Res Lett* 88:300–310. <https://doi.org/10.1785/0220160139>
- Cotton F, Archuleta R, Causse M (2013) What is Sigma of the stress drop? *Seismol Res Lett* 84:42–48. <https://doi.org/10.1785/0220120087>
- Dost B, van Eck T, Haak H (2004) Scaling of peak ground acceleration and peak ground velocity recorded in The Netherlands. *Neth Boll Geof Teor Appl* 45:153–168
- Drouet S, Cotton F (2015) Regional stochastic GMPE's in low-seismicity areas. Scaling and aleatoric variability analysis—application to the French Alps. *Bull Seismol Soc Am* 105:1883–1902. <https://doi.org/10.1785/0120140240>
- Ebel J, Wald D (2003) Bayesian estimations of peak ground acceleration and 5% damped spectral acceleration from modified mercalli intensity data. *Earthquake Spectra* 19:511–529
- Faenza L, Michelini A (2010) Regression analysis of MCS intensity and ground motion parameters in Italy and its application in ShakeMap. *Geophys J Int* 180:1138–1152. <https://doi.org/10.1111/j.1365-246X.2009.04467.x>
- Fischer T, Horálek J, Hrubcová P, Vavryčuk V, Bräuer K, Kämpf H (2014) Intra-continental earthquake swarms in West-Bohemia and Vogtland: a review. *Tectonophysics* 611:1–27. <https://doi.org/10.1016/j.tecto.2013.11.001>
- Grünthal G (1998) European macroseismic scale 1998 (EMS-98) cahiers du centre Européen de géodynamique et de séismologie 15. Centre Européen de géodynamique et de séismologie, Luxembourg
- Grünthal G, Wahlström R (2012) The European-Mediterranean earthquake catalogue (EMEC) for the last millennium. *J Seismol* 16:535–570. <https://doi.org/10.1007/s10950-012-9302-y>
- Grünthal G, Mayer-Rosa D, Lenhardt W (1998) Abschätzung der erdbebengefährdung für die D-A-CH-Staaten - Deutschland, Österreich, Schweiz. *Bautechnik* 75:753–767
- Heimann S (2011) A robust method to estimate kinematic earthquake source parameters. Dissertation, University of Hamburg. <http://ediss.sub.uni-hamburg.de/volltexte/2011/5357>
- Heimann S, Kriegerowski M, Isken M, Cesca S, Daout S, Grigoli F, Juretzek C, Megies T, Nooshiri N, Steinberg A, Sudhaus H, Vasyura-Bathke H, Willey T, Dahm T (2017) Pyrocko - an open-source seismology toolbox and library. V. 0.3. GFZ Data Services. <https://doi.org/10.5880/GFZ.2.1.2017.001>
- Hinzen K (2005) Ground motion parameters of the July 22, 2002, M_L 4.9 Alsdorf (Germany) earthquake. *Boll Geofis Teor Appl* 4:303–318
- Kämpf H et al (1991) Zur strukturellen Bedeutung der Nord-Süd-Bruchstörungszone Plauen/Klingenthal – Altenberg/Gera – Leipzig/Halle – Dessau/Bernburg, Tagungsband Geologisch-tektonischer Bau der Gera-Jachymov (Joachimsthal)-Störungszone und die daran gebundenen Uranlagerstätten, 04.-07. Aug. 1991 in Gera/Thüringen
- Korn M, Funke S, Wendt S (2008) Seismicity and seismotectonics of West Saxony, Germany—new insights from recent seismicity observed with the Saxonian seismic network. *Stud Geophys Geod* 52:479–492. <https://doi.org/10.1007/s11200-008-0033-z>
- Krawczyk CM, Stiller M, The DEKORP-BASIN Research Group (1999) Reflection seismic constraints on Palaeozoic crustal structure and Moho beneath the NE German Basin. *Tectonophysics* 314:241–253
- Lesueur C, Cara M, Scotti O, Schlupp A, Sira C (2013) Linking ground motion measurements and macroseismic observations in France: a case study based on accelerometric and macroseismic databases. *J Seismol* 17:313–333. <https://doi.org/10.1007/s10950-012-9319-2>

- Leydecker G (2011) Erdbebenkatalog für Deutschland mit Randgebieten für die Jahre 800 bis 2008. Geolog Jahrb. E:59 Bundesanstalt für Geowissenschaften und Rohstoffe, Hannover
- Mak S, Clements R, Schorlemmer D (2015) Validating intensity prediction equations for Italy by observations. *Bull Seismol Soc Am* 105:2942–2954. <https://doi.org/10.1785/0120150070>
- Murphy J, O'Brian L (1977) The correlation of peak ground acceleration amplitude with seismic intensity and other physical parameters. *Bull Seismol Soc Am* 67:877–915
- Oncescu MC, Camelbeeck T, Martin H (1994) Source parameters for the Roermond aftershocks of 1992 April 13 - May 2 and site spectra for P and S waves at the Belgian seismic network. *Geophys J Int* 116:673–682. <https://doi.org/10.1111/j.1365-246X.1994.tb03289.x>
- Ottmöller L, Voss P, Havskov J (2016) SEISAN earthquake analysis software for Windows, Solaris, Linux and MacOSX. User manual. <ftp://ftp.geo.uib.no/pub/seismo/SOFTWARE/SEISAN/seisan.pdf>
- Rappsilber I (ed) (2006) Halle-störung - mitteilungen zu geologie und bergwesen in Sachsen-Anhalt. vol 10, pp 1–154. Landesamt für Geologie und Bergwesen, Halle
- Richter CF (1958) Elementary seismology. W. H. Freeman and Company, San Francisco
- Rubin DB (1981) The Bayesian bootstrap. *Ann Stat* 9:130–134
- Sato T, Hirasawa T (1973) Body wave spectra from propagating shear cracks. *J Phys Earth* 21:415–431
- Schwarz J, Beinersdorf S, Meidow H, Ahorner L (2010) Magnitudenorientierter Erdbebenkatalog für deutsche und angrenzende Gebiete: EK DAG – erweiterte Katalog Version 1.0. Bauhaus Universität Weimar. https://www.edac.biz/fileadmin/Dokumente/04_Projekte/\discretionary-EKDAGv1.0-TeilB.pdf
- von Seebach K (1873) Das Mitteldeutsche Erdbeben vom 6. März 1872. Verlag von H. Haessel, Leipzig
- Takenaka H, Mameda Y, Futamura H (2003) Near-source effect on radiation pattern of high frequency S waves: strong SH-SV mixing observed from aftershocks of the 1997 Northwestern Kagoshima, Japan, earthquakes. *Phys Earth Planet Inter* 137:31–43. [https://doi.org/10.1016/S0031-9201\(03\)00006-2](https://doi.org/10.1016/S0031-9201(03)00006-2)
- Wald D, Quitariano V, Heaton H, Kanamori H, Scrivner CW, Worden CB (1999) Trinet 'shakemaps': rapid generation of peak ground motion and intensity maps for earthquakes in Southern California. *Earthq Spectra* 15:537
- Wald D, Quitariano V, Pankow KL (2006) Shakemap manual - Technical Manual, Userguide and Software Guide Tech. Report, USGS
- Wang R (1999) A simple orthonormalization method for stable and efficient computation of Green's functions. *Bull Seis Soc Am* 89:733–741
- Wang R, Heimann S, Zhang Y, Wang H, Dahm T (2017) Complete synthetic seismograms based on a spherical self-gravitating earth model with an atmosphere-oceanmantle-core structure. *Geophys J Int* 210:1739–1764. <https://doi.org/10.1093/gji/ggx259>
- Witthauer B (ed) (2016) Erdbebenbeobachtung in Mitteldeutschland, dreijahresbericht 2013–2015 landesamt für umwelt. Landwirtschaft und Geologie, Dresden